ACS APPLIED MATERIALS & INTERFACES

Research Article

www.acsami.org

Directional Liquid Spreading over Chemically Defined Radial Wettability Gradients

Olesya Bliznyuk,[†] James R.T. Seddon,[‡] Vasilisa Veligura,[†] E. Stefan Kooij,*[,†] Harold J. W. Zandvliet,[†] and Bene Poelsema[†]

[†]Physics of Interfaces and Nanomaterials and [‡]Physics of Fluids, MESA+ Institute for Nanotechnology, University of Twente, Enschede, The Netherlands

ABSTRACT: We investigate the motion of liquid droplets on chemically defined radial wettability gradients. The patterns consist of hydrophobic fluorinated self-assembled monolayers (SAMs) on oxidized silicon substrates. The design comprises a central hydrophobic circle of unpatterned SAMs surrounded by annular regions of radially oriented stripes of alternating wettability, i.e., hydrophilic and hydrophobic. Variation in the relative width of the stripes allows control over the macroscopic wettability. When a droplet is deposited in the middle, it will start to move over to the radially defined wettability gradient, away from the center because of the increasing relative surface area of hydrophilic matter for larger radii in the pattern. The focus of this article is on a qualitative description of the characteristic motion on such types of anisotropic patterns. The influence of design parameters such as pattern dimensions, steepness of the gradient, and connection between different areas on the behavior of the liquid are analyzed and discussed in terms of advancing and receding contact lines, contact angles, spatial extent, and overall velocity of the motion.

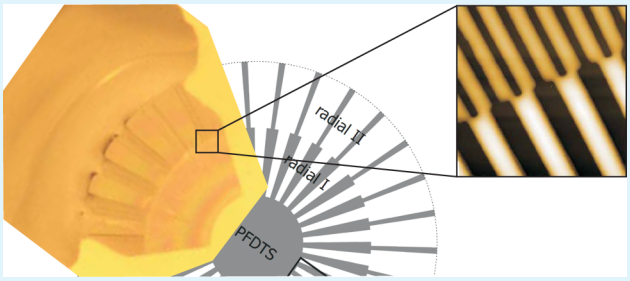

KEYWORDS: *directional wetting, surface energy gradient, self-assembled monolayers, liquid motion, microdroplets, inkjet printing*

INTRODUCTION

Ink jet printers encompass a popular choice both for household purposes as well as for many different industrial applications. For domestic use, the low price is a major advantage, whereas for industrial purposes, the versatility of the technology is of prime importance, enabling printing of a wide range of materials on various substrates.[1,2] Most recently, the possibilities of printing were even extended to three-dimensional objects.[3,4] The application areas for ink jet technology include displays,[5,6] the chemical industry,[7,8] electronic components,[9−12] and a large emerging field comprising the life sciences.[13,14] For all these applications, high speed and ultimate printing quality are required. This in turn has resulted in a lot of research activities in this area. Companies and research institutes developing the technology are faced with the challenge to further miniaturize and increase efficiency of the ink jet print heads.

The developments in silicon-based micro electro mechanical systems (MEMS) are presently also being applied to the ink jet technology. For instance, in 2008 27% of all inkjet printheads were fabricated using MEMS technologies. Despite the substantial investments initially required, many printing companies incorporate MEMS into their products for mass-production, since this technology enables achieving submicrometer resolution with high reliability, which is a must for large scale applications.[15] However, miniaturization of devices poses new challenges dictated by the fact that considerably more features have to be reproduced on markedly smaller surface areas.[16]

The way the droplets are created in a typical print head gives rise to small volumes of ink overflowing from the nozzles and ultimately wetting the nozzle plate.[2,17] Both metal and silicon nozzle plates are lyophilic for low surface tension inks, inhibiting complete removal of the residual ink by mechanical wiping. Accumulation of ink near the nozzle interferes with jetting of droplets and may lead to the interruption of jetting all together by blocking the nozzle.[18−20] This in turns leads to unreliable jetting behavior and is consequently detrimental for the print quality. Moreover, silicon nozzle plates as manufactured using MEMS technology exhibit wettability characteristics, which are strongly affected by ambient conditions such as temperature and humidity. Additionally, the silicon surface is easily contaminated therewith creating pinning sites which interfere with ink removal procedures.

A smart way to avoid undesired ink accumulation near the nozzle is to apply an antiwetting coating on the nozzle plate.[2,21,22] The surface is hydrophobized using a chemically inert agent, which allows easy removal of ink and reduces contamination. Presently, such an antiwetting coating is primarily applied as a single chemical species homogeneously deposited over the entire nozzle plate. However, it may be

Received: May 17, 2012
Accepted: July 27, 2012
Published: July 27, 2012

   dx.doi.org/10.1021/am3008856 | *ACS Appl. Mater. Interfaces* 2012, 4, 4141−4148

relevant to design patterns of more (typically two) chemical species with different surface energies, which will enable controlling ink movement on the nozzle plate, ultimately achieving a continuous flow of ink away from the nozzle. Despite the pioneering work on using surface energy gradients to control liquid motion, for example that of Chaudhury and Whitesides,[23] the inspiration to actually apply spatially varying wetting properties in modern technology to induce actuation of liquid droplets has only attracted increasing attention over the past 2 years. Both theoretical and experimental work has become focused on designing, manufacture and characterization of reliable, robust surfaces with well-defined wettability gradients.[24−32]

More generally, the topic of wetting of patterned surfaces comprises an extensive research field. The behavior of liquid droplets on anisotropically patterned surface is typically referred to as "directional wetting". Over the past decade a number of reviews have been written on the topic.[33−36] Anisotropic wetting characteristics give rise to different liquid spreading behavior in orthogonal directions. Such anisotropy can be induced either by morphological patterning, for example a grooved surface, or by chemical patterning with a specific directionality. In the former case, two wetting states often referred to as (i) Cassie−Baxter and (ii) Wenzel states are observed in which the liquid is elevated on top of surface asperities, or penetrates into the crevices, respectively. In the case of morphologically flat substrates with a spatially varying surface energy, the liquid is in all cases in contact with the entire surface.

By applying a gradient in the macroscopic wettability, it is in principle possible to induce liquid motion on such surfaces. A spatial gradient in surface energy is one way to passively control the movement of liquid in a specific direction. Alternatively, one can resort to active actuation using electrowetting, illumination or electrochemical means.[33] Recently, the ability to move liquids over linear wettability gradients, constituting chemically defined micrometer-sized stripes of alternating wettability has been demonstrated both experimentally and in simulations.[35,37−39] In this article, we present a study of liquid behavior on radially patterned surfaces. A surface free energy gradient induces droplet motion away from the point where it is deposited. We describe the patterns used to define the gradient and briefly indicate how they are made. A global description of the droplet motion is given, followed by a more detailed treatment of the receding motion. We also discuss the residual layer, which remains on the hydrophilic SiO_2 areas after the droplet has receded. The formation of single ridges of liquid as well as bridges covering up to 20 adjacent stripes at regular intervals and their influence on receding motion is presented. Finally, the influence of the radial pattern length on the velocity is discussed.

EXPERIMENTAL DETAILS

Surface Preparation. The surface patterns of self-assembled monolayers (SAMs) of 1H,1H,2H,2H-perfluorodecyltrichlorosilane (PFDTS, 97%, ABCR, Germany) on silicon wafers are created using standard clean room facilities. First, a positive photoresist is spin-coated on freshly cleaned wafers with a natural oxide film, followed by soft-baking. Patterns are created via standard optical lithography, after which the exposed photoresist is washed-off. The remaining photoresist is hard-baked and provides surface protection during vapor deposition of PFDTS; the silane headgroup binds covalently to the native silicon oxide, exposing the fluorinated tail to the liquid. The assembly creates a densely packed layer of molecules with a height in the order of one nanometer, on which glycerol has a stationary contact angle (CA) θ_{st} = 106°. Vapor deposition of PFDTS is done in a degassed chamber that is successively exposed to PFDTS and water reservoirs to introduce the respective vapors, initiating the reaction on the wafer surface.[40] After formation of the SAM, the photoresist is washed off, leaving a chemically patterned surface. The uncoated silicon oxide surface exposed after removing the photoresist exhibits typical static contact angles in the range of 30−40°, with receding angles of 10−15°.

Pattern Design. A wide range of different pattern designs was considered in this work. In total, thirty different designs were tested; reproducibility of the observations was verified on at least three different wafers. A typical layout used for the experiments is presented in Figure 1. The central circle is formed by a homogeneous unpatterned PFDTS SAM and has a diameter of 1.4 mm for all patterns studied. Droplets are always deposited on this circle. The circle diameter is chosen to be close to that of a 1 μL glycerol droplet on an unpatterned PFDTS SAM (1.39 mm). However, as deposition exactly in the middle of the circle cannot be achieved (patterns are not visible by the naked eye prior to wetting), the droplet will encounter the more hydrophilic part of the pattern before the equilibrium shape is reached. Consequently, the droplet will be pulled away from the center of the pattern and the translational motion is initiated. Surrounding the pure PFDTS circle are annular regions consisting of alternating hydrophobic (PFDTS) and hydrophilic (SiO_2) stripes with an increasing macroscopic surface energy. These create a preferential spreading direction for the droplets.[37] The fraction of hydrophilic surface area increases for radial sections further away from the center. We use a dimensionless parameter α to quantify the relative hydrophobicity of the pattern[41]

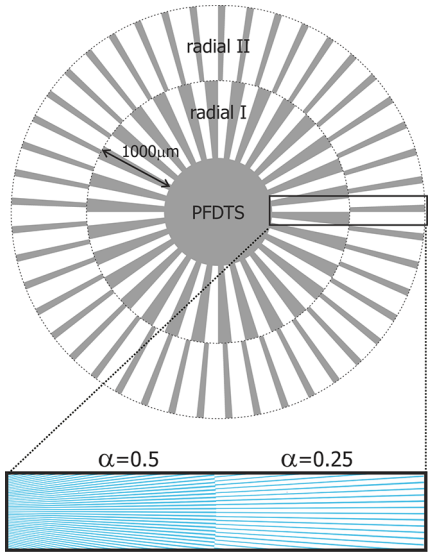

Figure 1. Schematic representation of a typical lithographic mask used to create the radial pattern on silicon wafers; note that the stripe widths are not to scale in the top image. The hydrophobic (PFDTS) and hydrophilic (SiO_2) regions correspond to the shaded and white areas, respectively. The wettability gradient is created by the transition from the homogeneous hydrophobic PFDTS central circle to the unpatterned SiO_2 via the annular radial patterns consisting of highly regular, radially directed stripes of alternating wettability. A pattern typically consists of two or three radial patterns with individual lengths of 700 or 1000 μm and hydrophobic-to-hydrophilic ratios α varying from 0.9 to 0.125. The enlargement depicts a section of the actual pattern. The width of the stripes is not uniform; with increasing distance from the center, the stripes become wider to maintain a constant value for α.

$$\alpha = \frac{w_{PFDTS}}{w_{SiO_2}} \quad (1)$$

where w_{PFDTS} and w_{SiO_2} are the hydrophobic PFDTS and hydrophilic SiO_2 stripe widths, respectively. Areas with smaller values for α correspond to larger overall surface energy, and as such are more hydrophilic. The range of α values considered in this work amounts to 0.9−0.125 for all radial patterns. As we will show in the following section, liquid motion is only induced for sufficiently steep gradients of α. Additionally, we also investigated patterns with continuously varying α values with increasing radial distance, for example by defining PFDTS lines of constant width; due to substantial pinning, these patterns did not induce sufficiently large forces to drive liquid away from the central region.

We employed two different types of pattern designs in terms of transition from one annular region to the next. In one case, the opening angle of the PFDTS stripes was the same for subsequent regions, and thus the opening angle of the SiO_2 stripes increased outward. In the other category, the opening angle of the SiO_2 stripes was the same (as shown in Figure 1), and the PFDTS width decreased. In both cases, this led to a mismatch of the periodicity of the stripes in two adjacent annular regions. As we will show, the mismatch leads to substantial pinning of the receding contact line.

Droplet Deposition. Droplet deposition is done using an OCA 15+ goniometer (DataPhysics, Germany), employing a computer-controlled syringe. We use glycerol (ReagentPlus, Sigma, USA) for all experiments, employing its high viscosity: it takes tens of seconds for droplets to move over the patterned surface. Unless otherwise specified, for all droplets the volume is fixed to 1 μL. The variation in droplet diameter just after being produced from the syringe was measured to be less than 5%. Deposition of the droplet is achieved by very slowly lowering the syringe with the suspended droplet toward the substrate until it contacts the patterned surface.[42]

A color camera is mounted above the deposition stage and is used to image the temporal evolution of the droplets over the patterned surface. Top-view movies are used to monitor and analyze droplet motion over the radial patterns. The top-view camera has a frame rate of 10fps, enabling a qualitative description of the slow movement of the glycerol droplets. After the outward movement of the droplet, a residual layer of glycerol remains on the patterned surface. The color movies provide a means to monitor this residual film.

The symmetry of the surface patterns with respect to the deposition point makes it virtually impossible to predict the direction of motion of droplets. Therefore, it is unfortunately not possible to quantitatively monitor the droplet kinetics using a (high-speed) side-view camera.

RESULTS

Droplet Advancing Motion Overview. As mentioned in the previous section, we investigated liquid motion on a range of samples with different pattern designs in terms of varying α and the radial length of the annular regions.

In Figure 2, the motion of a 1 μL glycerol droplet over a typical radial pattern is shown. The diameter of the central PFDTS circle is 1.4 mm; the two annular radial patterns in this case have α = 0.5 and α = 0.25 (referred to as radial I and radial II for the inner and outer area, respectively) and a length (i.e., the radial width of the annular region) of 1 mm each.

The direction of the outward motion is directly related to the precise position where the droplet first comes into contact with the central circle; deposition precisely in the center of the pattern is virtually impossible. If the initial contact of a completely symmetric droplet would be exactly in the middle of the pattern without any irregularities such as defects and dirt, no motion of the droplet center of mass is expected based on symmetry considerations.

In Figure 2a−c, straight sections of the contact line on the sides of the droplet can be observed due to pinning at the SiO_2 stripes. Their influence on the advancing motion is considered to be minimal due to their position at the trailing edge of the droplet. Overall, the advancing motion of the droplets on our radially striped patterns with well-defined structure exhibits marked similarities with the behavior of droplets on structureless energy gradient surfaces created by vapor deposition of molecules via diffusion-controlled process.[43,44] The droplets on the radial pattern are markedly more circular as opposed to those on linear wettability gradient arrays.[37] For the latter patterns, the confinement of the liquid between PFDTS stripes is stronger, forcing the liquid to move faster in the stripe direction as compared to the radial patterns considered in this work.

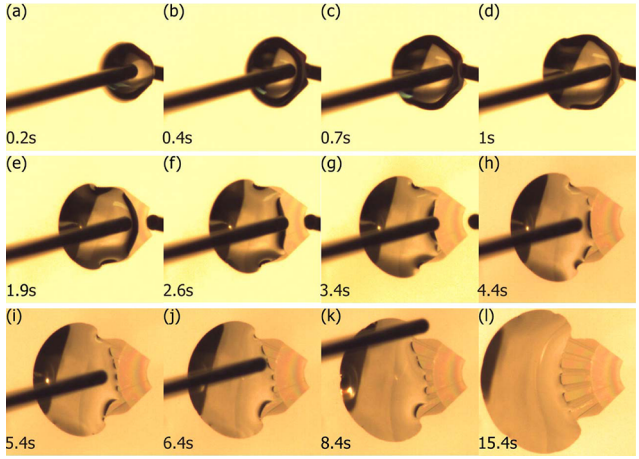

Figure 2. Motion of a 1 μL glycerol droplet over a typical radially patterned surface. The indicated times provide a global time scale. The unsharp edge of the droplet in the first four images is caused by the relatively high contact line velocity in relation to the shutter speed. (a−c) The advancing edge of the droplet wets both radial I and radial II, finally reaching the unpatterned SiO_2 on the outer perimeter of the pattern, followed by (d−f) dewetting of radial I. (g−l) Dewetting of radial II gives rise to liquid "bridges" of similar size at regular intervals.

Droplets Dewetting the Radial Pattern. The motion of the receding edge over the radial patterns is only observed when the advancing side starts to move over the unpatterned SiO_2 on the outer circumference of the pattern (Figure 2c). As the receding angle of glycerol on SiO_2 is very small, a thin layer remains on the SiO_2 stripes, which allows us to trace the way the droplet evolves over the patterned surface. In very recent experiments using liquids with different surface tension, the wettability contrast between the hydrophilic and hydrophobic stripes has proven to be a key parameter for the complete dewetting. Also, the pinning of the contact line on the SiO_2 stripes is important.

Initially, receding of the contact line is relatively fast over the PFDTS circle, followed by a considerable deceleration over the first annular region radial I. We assume this pronounced decrease in speed of the receding edge is due to the aforementioned pinning on the SiO_2 stripes. Pinning may well originate from the nonideal structure of the PFDTS edges, inhomogeneities and/or impurities. As a result, an unfavorable convex curvature on the edge of the pure PFDTS circle and two strongly curved corners, representing a high unbalanced Laplace pressure, are formed on the receding side of the droplet. Due to the presence of these features, the receding velocity of the contact line is not homogeneous. Initially, the motion is observed only at the sharply curved corner regions,

dx.doi.org/10.1021/am3008856 | ACS Appl. Mater. Interfaces 2012, 4, 4141−4148

whereas the center of the receding contact line remains pinned at the edge of the circular PFDTS region. However, this inhomogeneity in receding velocities along the contact line enables the droplet to adopt a more favorable shape with a convex receding contact line.

The convex shape of the contact line will reappear when the contact line is pinned on the chemically defined border between the two annular regions, referred to as radial I and radial II (Figure 2g). Meanwhile, spreading over the SiO_2 continues and the droplet volume is steadily being pulled off the patterned surface, forcing the receding edge to eventually move away from the outer patterned area designated as radial II.

The droplet receding from the second annular pattern exhibits features, which are emphasized by using a large volume droplet (Figure 3). Specifically, the formation of the regularly spaced, symmetric liquid "bridges", covering up to ten periods (one period comprises a hydrophobic PFDTS and a hydrophilic SiO_2 stripe) is observed in Figure 2h–l. Both the width and the specific location of these liquid bridges are reproducible on the same pattern.

A consequence of the formation of these so-called bridges, i.e., a discontinuous depinning of the receding contact line from the chemical border between radial I and radial II, is that an unambiguous definition of the overall receding velocity of the liquid is difficult. Along the entire contact line, in some places the receding part of the contact line (between the bridges) already moves, whereas in outer locations, it is still pinned. For example, the liquid totally recedes from the pattern in areas close to the droplet edge while in the middle it is still fully covering the radial II (Figure 2j, k). To enable assessment of the time scale for the liquid to recede over radial II, we choose to define the duration of the receding motion to start once the last receding part becomes depinned from the border between radial I and II until the droplet completely dewets the regions between the bridges.

When considering the time it takes for the droplet to dewet each respective radial pattern, this may explain the absence of bridges on the first annular region, i.e., radial I, and also for the difference in average velocities of the receding motion. In case of the 1 μL droplets, the time span to dewet radial I is typically of the order of 3 s, whereas it takes close to 10 s to dewet radial II.

Ultimately, the droplet completely dewets the radial pattern. Nevertheless, a small amount of liquid remains on the SiO_2 stripes of radial II and also in the liquid bridges, both exhibiting a thickness in the micrometer range. A thin continuous layer of glycerol remaining on individual SiO_2 stripes is stable and does not decay with time. Discontinuities in coverage do not induce liquid rearrangements either, as can be seen on the enlarged image of the liquid trace as presented in Figure 3. In a few interbridge spaces, bright spots (one being indicated by white arrow) correspond to liquid-free surface areas.

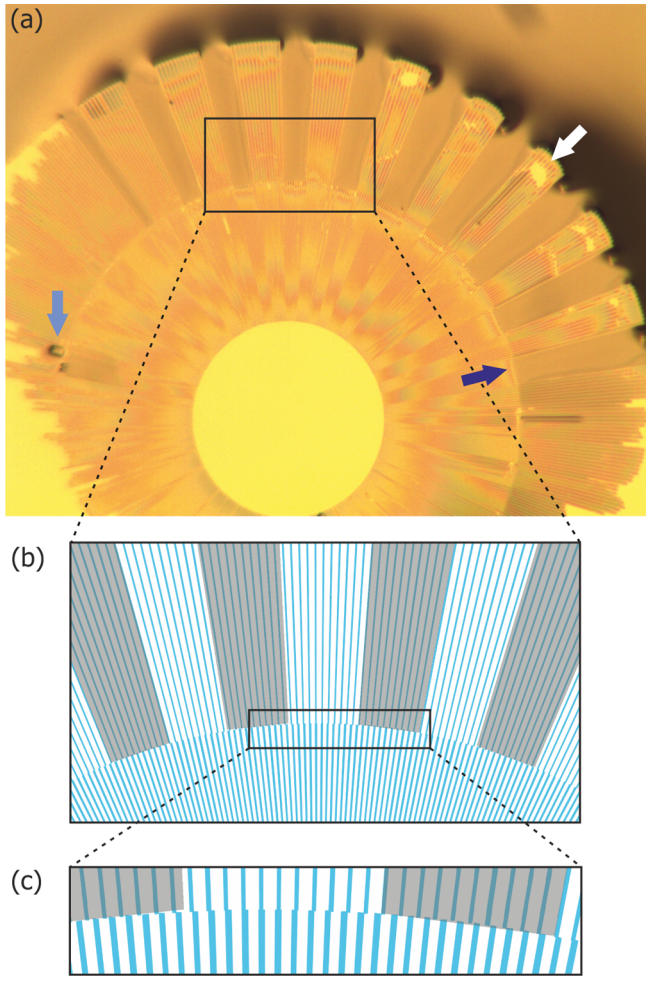

Figure 3. (a) Image of a radial pattern with glycerol remaining on the SiO_2 stripes after a 5 μL droplet has moved outward. The image is obtained 5–10 min minutes after initial deposition. Using large volume droplets highlights characteristic features for these anisotropic patterns. Among these are what we refer to as "bridges"; the blue arrow (bottom right) indicates one of the liquid bridges on radial II. The white arrow shows a discontinuity in the wetted SiO_2 stripes. The light-blue arrow (left) indicates a "square" droplet formed by receding of the unstable bridge covering two SiO_2 and one PFDTS stripes. (b) Section of the lithographic mask showing the spatial locations where liquid bridges are observed (indicated by the shaded areas). For this particular pattern, the bridges, on average, cover ten periods of the pattern and are spaced ten periods apart. (c) Enlargement of the border between radial I and radial II showing the connection between stripes in the two annular regions.

DISCUSSION

Residual Liquid Ridges on Radially Patterned Surfaces. As mentioned in the previous section, the combination of a low receding CA on the SiO_2 stripes and the low vapor pressure of glycerol leads to a thin stable residual layer of liquid on the hydrophilic stripes after the bulk of the droplet has receded. Atomic force microscopy (AFM) was used to study the height of the remaining liquid layer on radial I; a typical image of the transition between radial I and II is shown in the top panel of Figure 4. The height variation for individual liquid ridges covering a SiO_2 stripe is presented in the bottom of Figure 4. As the stripe becomes wider, an increase of the maximum height of the liquid is observed, ranging from approximately 500 nm at the beginning of the stripe to 1.3 μm for the broader end of the stripe.

Assuming that we can represent the cross section of the ridge by a circular profile, the height variation with stripe width follows directly from the geometry. The CAs of the glycerol ridge at the chemically defined edges between glycerol-covered SiO_2 stripes and liquid-free PFDTS stripes were determined from the aforementioned circular profile fits at different positions along the residual liquid stripes. Typically, the CA amounts to $\theta \approx 17°$ for the entire length of the ridge. Because

dx.doi.org/10.1021/am3008856 | ACS Appl. Mater. Interfaces 2012, 4, 4141–4148

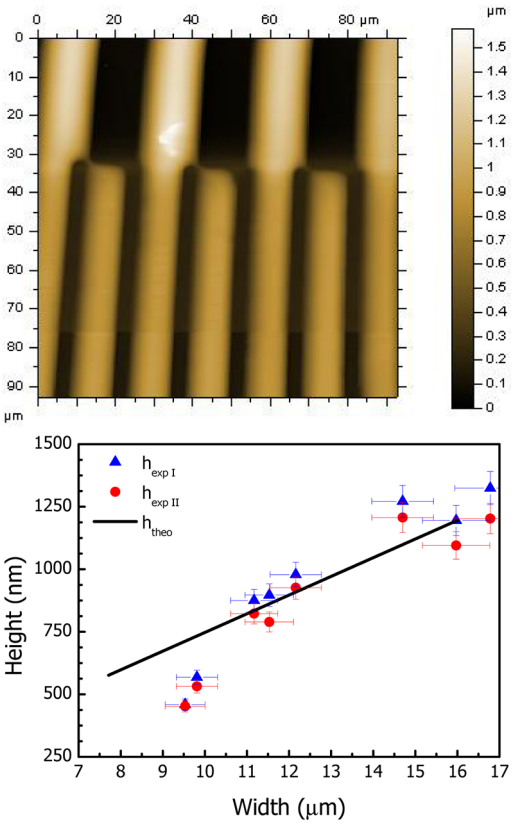

Figure 4. (top) Atomic force microscope (AFM) image (93 μm × 93 μm) of residual glycerol ridges covering SiO_2 stripes. The image is taken at the border between radial I (upper "wider" lines) and radial II (bottom "thinner" lines), in the region where the SiO_2 stripes of two patterns are connected. The measurements were done exclusively on the ridges present on radial I, most of which are not shown here. (bottom) Plot of experimentally measured heights of two ridges covering a single SiO_2 stripe. The solid line depicts the theoretical calculation (2) as described in the text.

the system is in equilibrium, the specific value of the contact angle is indeed expected to be the same over the entire length; the precise value is dictated by the Young's balance on the underlying SiO_2 substrate. We consider it to be slightly higher than the receding angle of glycerol on silicon oxide surfaces. Control experiments on a pure SiO_2 wafer using an optical contact angle goniometer verify that indeed the receding angles for glycerol are in the range of 10−15°. The experimental CA values are considerably smaller than 90°, which is in agreement with the stability condition for liquid ridges on chemically defined stripes.[45,46]

Straightforward geometrical considerations including a circular segment profile provide a simple expression of the height of the ridge, given by

$$h = \frac{w_{SiO_2}(1 - \cos\theta)}{2\sin\theta} \qquad (2)$$

where θ corresponds to the glycerol CA and w_{SiO_2} is the width of the SiO_2 stripe. The calculated height using $\theta = 17°$ as plotted by the solid line in Figure 4 is in good agreement with the experimentally observed heights for the most of the ridge length. However, at the end of the liquid ridge, the measured heights are smaller than the calculated values. The curvature at the terminating outer end of the liquid "finger" gives rise to lower values for the CA and thus smaller heights.

Liquid Bridges. As described in relation to Figures 2 and 3, regularly spaced, similarly sized liquid bridges covering a number of periods of the underlying pattern are typically observed on all radial patterns. A better understanding why these bridges occur and why they are stable is of interest in particular for future pattern designs in relation to potential applications.

The result as presented in Figure 3 was obtained a few minutes after the droplet has moved over the pattern. As such, this allows studying the liquid in a static state, without the influence of moving contact lines. The system attempts to achieve the energetically most favorable configuration by allowing the excess liquid to wet the available hydrophilic surface area, i.e., the stripes. However, the so-called bridges persist on a time scale exceeding the measurement duration without showing any sign of disintegration and dewetting of the hydrophobic PFDTS stripes underneath these bridges. Moreover, by comparing results obtained on different radial patterns, we find that these bridges have varying widths and spacings depending on the precise design of the underlying pattern.

An interesting observation is that none of the patterns show bridge formation on the first annular region. On the other hand, all patterns exhibit formation of regularly spaced bridges on the second annular region radial II. In cases where a third annular region is present, bridge formation also occurs on these. The bridges can easily be identified in the top-view images such as those in Figure 2 or Figure 3a.

In an attempt to understand the occurrence of bridges on the second annular region, we depict enlargements of a part of the pattern in Figure 3b,c. The similar sizes and regular positions of liquid bridges suggest that the reason for their presence is most likely related to a repeatedly occurring feature in the pattern. By overlaying the top-view images with the lithographically defined pattern, as we have done in Figure 5, it becomes clear that the bridges are observed in those places where the hydrophobic and hydrophilic stripes of radial I and radial II are not connected, i.e. where the periodicity of both patterns is out of registry. Because of the different α values in the two regions the periodicity of the stripes is different, and as such the relative positions of the stripes shift with respect to each other. In the region between the bridges the hydrophilic stripes of radial I connect to the hydrophobic stripes of radial II.

At the border between the PFDTS circle and radial I, as schematically shown in Figure 5a, the receding contact line is pinned. As soon as the receding CA value for a given α is reached, receding motion of the contact line will be initiated. Owing to the symmetry of the system, the receding motion is similar along the entire border between radial I and the PFDTS circle. However, once the contact line becomes pinned at the beginning of radial II, as schematically shown in Figure 5b, not only the fraction of hydrophilic surface area on radial II is higher, therewith lowering the macroscopic receding CA, but also the shape of the contact line is markedly different and not homogeneous along the border. In the regions where the bridges are not formed, i.e., where the SiO_2 stripes of both regions connect (see also Figure 5c), the contact line exhibits a regular corrugation and more or less experiences a continuous pattern, albeit with a lower α.

On the other hand, in the regions where bridges are formed, the hydrophobic stripes in radial II originate where hydrophilic stripes of radial I end. This perturbs the contact line structure,

dx.doi.org/10.1021/am3008856 | ACS Appl. Mater. Interfaces 2012, 4, 4141−4148

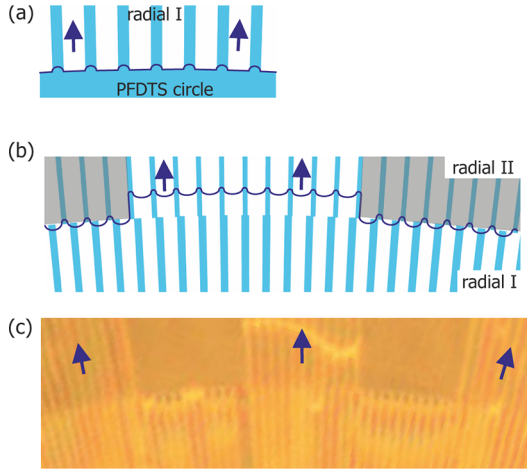

Figure 5. Schematic representations of pinning of the receding contact line at the chemical border (a) between the central PFDTS circle and radial I, and (b) between radial I and radial II. In (b) a part of the pattern is shown where bridge formation is inhibited (center) and neighboring regions where bridges are formed. The bridges are schematically indicated by the shaded rectangle. The shaded (blue) lines correspond to hydrophobic PFDTS, while white represents the hydrophilic SiO_2 surface. The arrows indicate the direction of contact line motion. (c) Enlargement of a top-view image of an actual wetted surface, showing the bridges; the regions where patterns in radial I and II are in registry are indicated by the (blue) arrows.

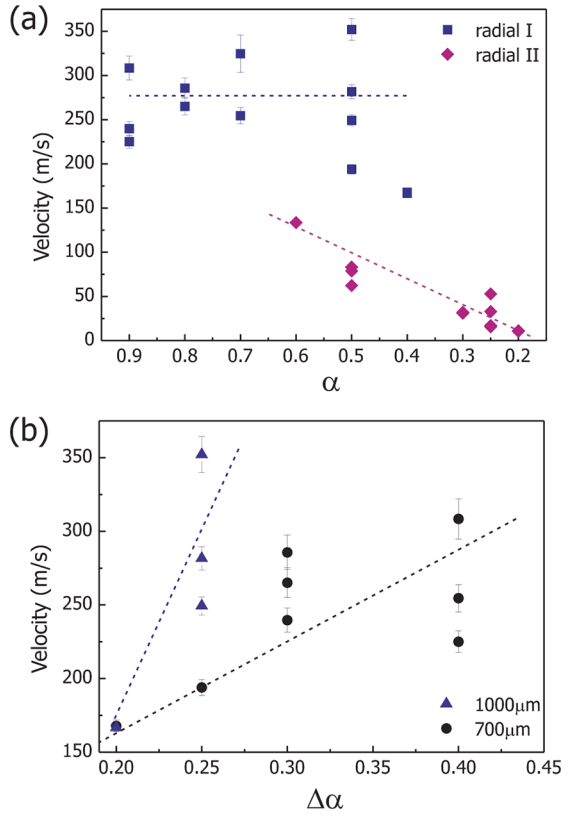

Figure 6. (a) Experimental dewetting velocities for 1 μL glycerol droplets over the radially patterned surfaces. The α-values are plotted on an inverse scale matching their evolution with increasing radial distance in the patterns. The moment of depinning is taken when the contact line completely detaches from the border. The moment of depinning is defined within three frames, corresponding to an error of 0.3*s*. The error bars for velocities on radial II are not discernible because of the large time scale. (b) Average velocity of the receding contact line over radial I as a function of the difference in α-values between radial I and radial II, in relation to the radial length of the pattern. The dashed lines represent trend lines, serving as a guide to the eye.

and as such gives rise to substantial pinning and thus bridge formation. Further enlargement of the border between the two regions (as shown in Figures 3c and 5b) reveals a critical mismatch between the respective hydrophobic stripes that will lead to bridge formation. In this particular example, the bridges are stable as long as the PFDTS stripes of radial I are not connected to ones of radial II. In some cases, the bridges persist even when the PFDTS stripes are connected, but still very close with a small gap. Most likely, this is related to limitations of the lithographic process. The mask shows sharply defined edges, but in the actual pattern the photoresist will smoothen out the features to some extent, creating a more gradual transition and allowing liquid to stay connected for the SiO_2 stripes.

Overall, we conclude that bridges are stable in areas where the hydrophobic stripes of the subsequent, outer radial pattern are not connected to the ones of the more inner radial region. When the hydrophobic sections of neighboring striped regions are in registry, the corrugation of the contact line is sufficient to initiate its receding motion. These findings are in line with the general principle[47,48] that changes in the wettability of a surface that are perpendicular to the contact line tend to cause pinning, whereas changes that are parallel to the contact line tend not to cause pinning.

Surface Energy Dependence of the Receding Motion. To enable a comparison of the difference in time scales of dewetting of patterns with different surface energies represented by various α-values for radial I and radial II, in Figure 6 we plot the velocities of the contact line as determined from the top-view movies. We assume that the receding motion starts once the entire contact line has depinned (dewetting of radial I) or once the last of the separated regions between the bridges starts to recede (dewetting radial II and radial III). The receding motion over a specific radial region is considered to end when the droplet has completely receded from the specific radial pattern. The time span defined in this way is divided by the known length of the pattern, therewith obtaining an average velocity. By presenting these average velocities as a function of α enables us to compare patterns with various lengths for radial I and radial II, as well as different combinations of α_I and α_{II} in a single graph.

The data in Figure 6a show that the receding velocities for the first radial pattern I are similar for different α values, but the scatter of the data is significant. A velocity increase for larger α values can be discerned for radial II but more experimental data is required for confirmation and identification of a specific trend. Comparing the velocities over radial I and II for different pattern designs reveals a marked difference. Velocities over the outer annular region are consistently lower, which we ascribe to the increasing width of the droplet.

To study whether the influence of the pattern length as well as variation of the α-value for radial II has influence on receding motion over radial I, in Figure 6b, we plot the average velocities of the receding contact line as a function of $\Delta\alpha = \alpha_I - \alpha_{II}$. Results on pattern designs with two different lengths (1000 and 700 μm) are indicated by different symbols. For both pattern lengths the results show an increase of the velocity for larger differences $\Delta\alpha$ between the two radial regions. Such an increase is in agreement with expectations, as a larger $\Delta\alpha$ implies a

dx.doi.org/10.1021/am3008856 | ACS Appl. Mater. Interfaces 2012, 4, 4141−4148

larger difference in surface energies and corresponding driving force, ultimately leading to the faster movement of the droplet to the more favorable areas on the surface.

Unfortunately, because of the considerable scatter of the experimental data, it is difficult to draw conclusions concerning the influence of the pattern length on the velocities. The present results on a limited number of patterns indicate that the velocities are higher for patterns with 1000 μm radial pattern length. More data are needed to enable a full quantitative analysis; this lies outside the scope of this work.

CONCLUSIONS

Inspired by potential application in inkjet printing technology, a qualitative description of glycerol droplet motion over radially patterned, chemically functionalized surfaces has been presented. The patterns considered in this article consist of a hydrophobic PFDTS circle in the center of the design, surrounded by annular striped regions consisting of radially oriented stripes of alternating wettabilities, i.e,. hydrophilic and hydrophobic. The anisotropic surface patterning creates a preferential direction for droplet motion away from the hydrophobic center circle onto the hydrophilic unpatterned silicon oxide around the pattern. The relative widths of the stripes (in the micrometer range) were varied to study droplet behavior on patterns with variable macroscopic surface energies. The experimental results can be compared with previous observations on linear patterns on which quantitative studies were carried out. Similarities as well as differences between the radial and linear patterns have been described and discussed. Comparing the receding velocities, we find that overall the motion over radial patterns is slower as compared to that over the linear designs. Most likely, this difference originates from the fact that, as compared to the linear patterns, the radial patterns impose a less strict confinement of the liquid (by the hydrophobic PFDTS stripes) in the direction perpendicular to the motion of the liquid. Furthermore, specific features observed on radial patterns, such as liquid bridges and residual liquid layers on individual hydrophilic stripes that remain after the droplet has receded over the pattern, are discussed to identify their origin and with the distant goal to avoid their formation in future pattern designs.

AUTHOR INFORMATION

Corresponding Author

*E-mail: e.s.kooij@utwente.nl.

Notes

The authors declare no competing financial interest.

ACKNOWLEDGMENTS

We thank Gor Manukyan (University of Twente, Physics of Complex Fluids) for assistance with the PFDTS coating on the wafers. We gratefully acknowledge the support by MicroNed, a consortium to nurture microsystems-technology in The Netherlands.

REFERENCES

(1) Williams, C. *Phys. World* **2006**, *19*, 24−29.
(2) Wijshoff, H. *Phys. Rep.* **2010**, *491*, 77−177.
(3) Lewis, J. A. *Adv. Funct. Mater.* **2006**, *16*, 2193−2204.
(4) Pataky, K.; Braschler, T.; Negro, A.; Renaud, P.; Lutolf, M. P.; Brugger, J. *Adv. Mater.* **2012**, *24*, 391.
(5) Hwang, J. Y.; Chien, L. C. Multi-Domain Liquid Crystal Alignment Based on Periodical Polyimide Micro-Bars Fabricated by Inkjet Printing. In *Proceedings of Emerging Liquid Crystal Technologies V*; SPIE-International Society for Optical Engineering: Bellingham, WA, 2010; Vol. *7618*.
(6) Chen, C. T.; Wu, K. H.; Lu, C. F.; Shieh, F. *J. Micromech. Microeng.* **2010**, *20*, 055004.
(7) Fousseret, B.; Mougenot, M.; Rossignol, F.; Baumard, J. F.; Soulestin, B.; Boissiere, C.; Ribot, F.; Jalabert, D.; Carrion, C.; Sanchez, C.; Lejeune, M. *Chem. Mater.* **2010**, *22*, 3875−3883.
(8) Beccherelli, R.; Zampetti, E.; Pantalei, S.; Bernabei, M.; Persaud, K. C. *Sens. Actuator B-Chem.* **2010**, *146*, 446−452.
(9) Cheng, Z. Y.; Xing, R. B.; Hou, Z. Y.; Huang, S. S.; Lin, J. *J. Phys. Chem. C* **2010**, *114*, 9883−9888.
(10) Delaney, J. T.; Liberski, A. R.; Perelaer, J.; Schubert, U. S. *Macromol. Rapid Commun.* **2010**, *31*, 1970−1976.
(11) Loffredo, F.; Del Mauro, A. D.; Burrasca, G.; La Ferrara, V.; Quercia, L.; Massera, E.; Di Francia, G.; Sala, D. D. *Sens. Actuators, B* **2009**, *143*, 421−429.
(12) Wu, Y.; Girgis, E.; Strom, V.; Voit, W.; Belova, L.; Rao, K. V. *Phys. Status Solidi A* **2010**, *208*, 206−209.
(13) Cui, X. F.; Dean, D.; Ruggeri, Z. M.; Boland, T. *Biotechnol. Bioeng.* **2010**, *106*, 963−969.
(14) Desai, S.; Perkins, J.; Harrison, B. S.; Sankar, J. *Mater. Sci. Eng., B* **2010**, *168*, 127−131.
(15) MEMS Inkjet printheads: new developments for growing industrial applications. Jan 2009; http://www.yole.fr/pagesAn/micronews/newslett.asp.
(16) Menzel, C.; Bibl, A.; Hoisington, P. MEMS solutions for precision micro-fluidic dispensing application. In *NIP20: International Conference on Digital Printing Technologies*; Salt Lake City, UT, Oct 2004 ; Society for Imaging Science and Technology: Springfield, VA, 2004; Vol. *20*; pp 169−175.
(17) Jong de, J.; Bruin de, G.; Reinten, H.; Berg van den, M.; Wijshoff, H.; Versluis, M.; Lohse, D. *J. Acoust. Soc. Am.* **2006**, *120*, 1257−1265.
(18) Beulen, B.; de Jong, J.; Reinten, H.; van den Berg, M.; Wijshoff, H.; van Dongen, R. *Exp. Fluids* **2007**, *42*, 217−224.
(19) de Jong, J.; Reinten, H.; Wijshoff, H.; van den Berg, M.; Delescen, K.; van Dongen, R.; Mugele, F.; Versluis, M.; Lohse, D. *Appl. Phys. Lett.* **2007**, *91*, 204102.
(20) van der Bos, A.; Segers, T.; Jeurissen, R.; van den Berg, M.; Reinten, H.; Wijshoff, H.; Versluis, M.; Lohse, D. *Appl. Phys. Lett.* **2011**, *110*, 034503.
(21) Chen, Y. M.; Mertz, R.; Kulenovic, R. *Int. J. Multiphase Flow* **2009**, *35*, 66−77.
(22) Chun-Fu, L.; Wen-Chieh, L.; Chun-Jung, C.; Chien-Chung, F. Anti-wetting trench of nozzle plate for piezoelectric actuating dispenser. In *4th International Microsystems, Packaging, Assembly and Circuits Technology Conference (IMPACT 2009)*; Taipei, Taiwan, Oct 21−23, 2009 ; .Institute of Electrical and Electronics Engineers (IEEE): Piscataway, NJ, 2009; pp 674−677.
(23) Chaudhury, M. K.; Whitesides, G. M. *Science* **1992**, *256*, 1539.
(24) Hong, D.; Cho, W. K.; Kong, B.; Choi, I. S. *Langmuir* **2010**, *26*, 15080.
(25) Das, A. K.; Das, P. K. *Langmuir* **2010**, *26*, 15883.
(26) Wu, J.; Ma, R.; Wang, Z.; Yao, S. *Appl. Phys. Lett.* **2011**, *98*, 204104.
(27) Zhang, Y.; Pi, P. H.; Wen, X. F.; Zheng, D. F.; Cai, Z. Q.; Cheng, J. *Prog. Chem.* **2011**, *23*, 2457.
(28) Neuhaus, S.; Padesta, C.; Spencer, N. D. *Langmuir* **2011**, *27*, 6855.
(29) Hao, P. F.; Lv, C. J.; Zhang, X. W.; Yao, Z. H.; He, F. *Chem. Eng. Sci.* **2011**, *66*, 2118.
(30) Moosavi, A.; Mohammadi, A. *J. Phys.: Condens. Matter* **2011**, *23*, 085004.
(31) Neuhaus, S.; Spencer, N. D.; Padeste, C. *ACS Appl. Mater. Interface* **2012**, *4*, 123.
(32) Xu, X.; Qian, T. *Phys. Rev. E* **2012**, *85*, 051601.
(33) Darhuber, A. A.; Troian, S. M. *Annu. Rev. Fluid Mech.* **2005**, *37*, 425.

(34) Herminghaus, S.; Brinkmann, M.; Seemann, R. *Annu. Rev. Mater. Res.* **2008**, *38*, 101.
(35) Xia, D.; Johnson, L. M.; Lopez, G. P. *Adv. Mater.* **2012**, *24*, 1287−1302.
(36) Hancock, M. J.; Sekeroglu, K.; Demirel, M. C. *Adv. Funct. Mater.* **2012**, *22*, 2223.
(37) Bliznyuk, O.; Jansen, H. P.; Kooij, E. S.; Zandvliet, H. J. W.; Poelsema, B. *Langmuir* **2011**, *27*, 11238−11245.
(38) David, R.; Neumann, A. W. *Colloids Surf., A* **2012**, *399*, 41−45.
(39) David, R.; Neumann, A. W. *Colloids Surf., A* **2012**, *393*, 32−36.
(40) Rathgen, H. Superhydrophobic surfaces: from fluid mechanics to optics. *Ph.D. Thesis*, University of Twente, Enschede, The Netherlands, 2008.
(41) Bliznyuk, O.; Vereshchagina, E.; Kooij, E. S.; Poelsema, B. *Phys. Rev. E* **2009**, *79*, 041601.
(42) Bliznyuk, O.; Jansen, H. P.; Kooij, E. S.; Poelsema, B. *Langmuir* **2010**, *26*, 6328−6334.
(43) Elwing, H.; Welin, S.; Askendal, A.; Nilsson, U.; Lundstrom, I. *J. Colloid Interface Sci.* **1987**, *119*, 203−210.
(44) Hlady, V.; Golander, C.; Andrade, J. D. *Colloids Surf.* **1988**, *33*, 185−190.
(45) Mechkov, S.; Rauscher, M.; Dietrich, S. *Phys. Rev. E* **2008**, *77*, 061605.
(46) Brinkmann, M.; Kierfeld, J.; Lipowsky, R. *J. Phys. A* **2004**, *37*, 11547.
(47) Johnson, R. E.; Dettre, R. H. *J. Phys. Chem.* **1964**, *68*, 1744.
(48) Kusumaatmaja, H.; Vrancken, R. J.; Bastiaansen, C. W. M.; Yeomans, J. M. *Langmuir* **2008**, *24*, 7299.